1273 K–100 MPa creep

	$t = 15.6$ h	$t = 131.3$ h	$t = 137.5$ h

γ' morphology

γ

γ'

[001]

[100]

[010]

strain rate

$\dot{\overline{\varepsilon}}^{\mathrm{p}} + \dot{\overline{\varepsilon}}^{\mathrm{c}}$

$(10^{-8}\mathrm{s}^{-1})$

8.89

5.93

2.96
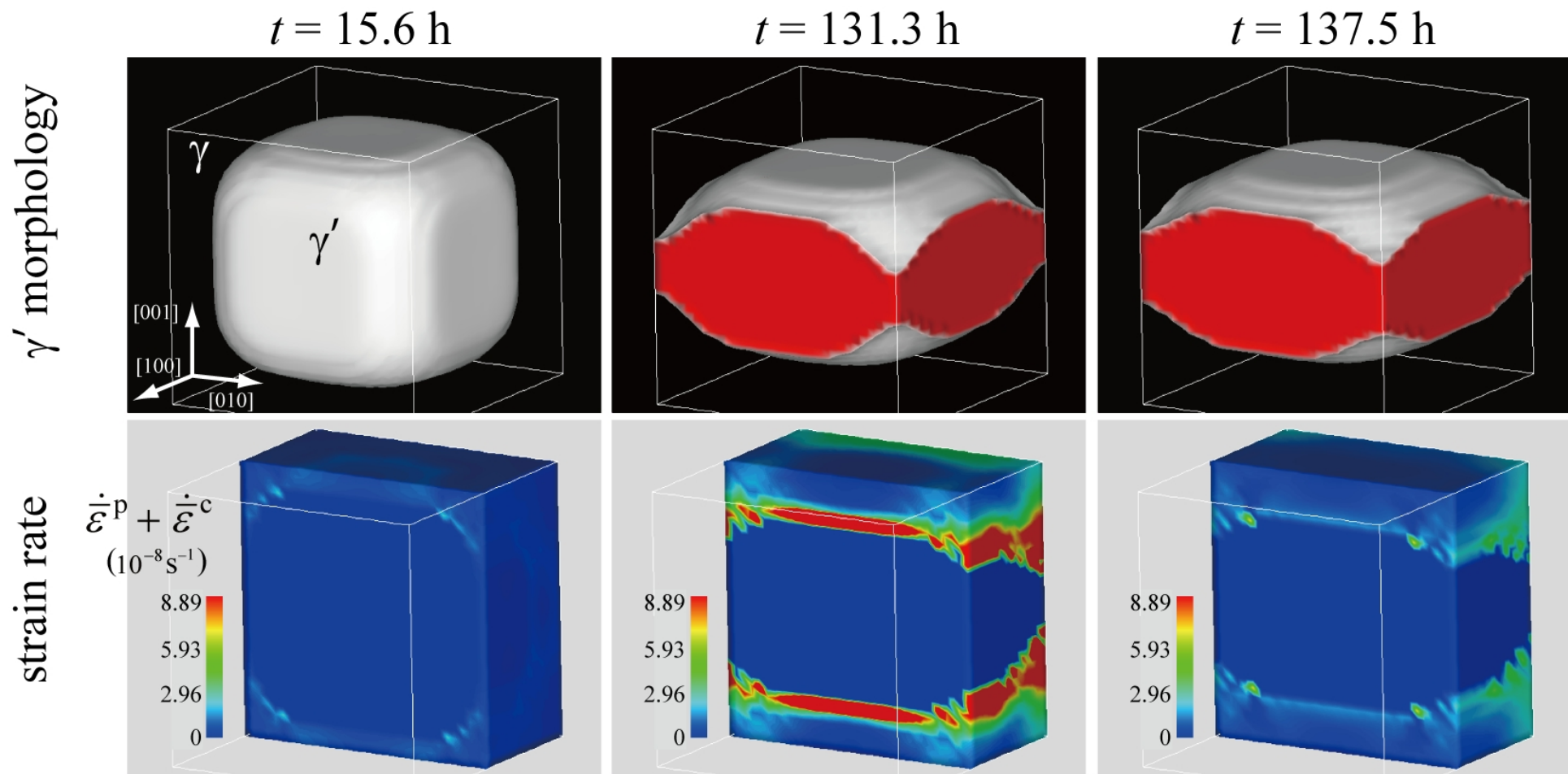
0

Title:

Phase-field simulation of rafting kinetics in a nickel-based single crystal superalloy

Author names:

Yuhki TSUKADA[a,b,*], Toshiyuki KOYAMA[a], Fuminori KUBOTA[c], Yoshinori MURATA[a], Yoshihiro KONDO[d]

Affiliations:

[a]   Department of Materials, Physics and Energy Engineering, Graduate School of Engineering, Nagoya University, Furo-cho, Chikusa-ku, Nagoya 464-8603, Japan

[b]   JST, PRESTO, 4-1-8 Honcho, Kawaguchi, Saitama 332-0012, Japan

[c]   Department of Materials Science and Engineering, Graduate School of Engineering, Nagoya Institute of Technology, Gokiso-cho, Showa-ku, Nagoya 466-8555, Japan

[d]   Department of Mechanical Systems Engineering, School of Systems Engineering, National Defense Academy, 1-10-20 Hashirimizu, Yokosuka 239-8686, Japan

[*]Corresponding author:

　　　Tel.: +81-52-789-3228

　　　E-mail address: tsukada@numse.nagoya-u.ac.jp

Abstract

Directional coarsening (rafting) of the γ' precipitate phase during creep in a nickel-based single crystal superalloy is simulated using the phase-field method. Both the morphological change of the γ' phase and the microstructure-dependent heterogeneous creep of the γ matrix phase are modeled in the simulation. In three-dimensional simulations considering a single γ' particle at 1273 K under tensile stresses of 130 MPa and 100 MPa along the [001] crystallographic direction, the γ' phase coarsens toward the direction perpendicular to the applied stress axis. The simulated macroscopic creep rate–time curve in the initial stage of creep is consistent with the experimental data. The time to rafting increases with decreasing magnitude of the applied external stress. Furthermore, the external stress is removed at an arbitrary strain in the simulation at 1273 K, and the occurrence of rafting during the subsequent heat treatment without external stress is confirmed. The simulation results show that the threshold value of macroscopic strain for inducing rafting (ε_{th}) is $\varepsilon_{th} = 0.12\%$–$0.16\%$ in the stress range of 100–160 MPa. Moreover, rafting can be accelerated by removing the external stress of 100–160 MPa when the macroscopic strain exceeds ε_{th}.

1. Introduction

Nickel-based single crystal superalloys are currently used in gas turbines for aerospace or land-based power plant applications because they exhibit superior creep strength at high temperatures [1]. The excellent mechanical properties of superalloys are derived from the cuboidal γ' strengthening phase, which coherently precipitates in the γ phase. The creep rupture life of superalloys is influenced by the microstructure evolution during the creep, i.e., the morphological change of the γ' phase. In the initial stage of the high-temperature creep of the commercial CMSX-4 alloy, the cuboidal γ' phase aligned along the ⟨001⟩ crystallographic directions coarsens toward the direction perpendicular to the [001] tensile stress axis. This phenomenon is called directional coarsening or "rafting" [2]. Several studies have investigated the rafting phenomenon using phase-field simulations [3-15], revealing that plasticity in the γ phase is the main driving force for rafting. This is consistent with the experimental observations of Matan et al. [16], who showed that rafting occurs during the heat treatment of pre-crept samples even in the absence of an external stress. A similar experimental result was obtained by Véron et al. [17], who observed the occurrence of rafting in the strained zone around an indentation after aging (strain-induced rafting). On the other hand, Matan et al. [16] showed that there exists a threshold strain (ε_{th}) for inducing rafting; if the macroscopic strain magnitude is below ε_{th}, rafting is not observed after the removal of external stress. Precise knowledge of the rate of rafting at high temperatures with and without external stress and of the effect of the magnitude of creep stress on ε_{th} is considered to be important for microstructure-based design of superalloys.

Above $0.6T_{\text{m}}$, where T_{m} is the absolute melting temperature, creep (time-dependent plasticity) occurs by a combined climb-plus-glide mechanism; when a gliding dislocation is pinned, a small amount of climb can release it, allowing a further glide to occur [1,18]. The dislocation climb occurs by lattice diffusion, and hence, is a thermally activated process.

Although a phase-field model that calculates dislocation dynamics (or evolution of dislocation density field) of specific slip systems in crystalline materials does exist [10,19,20], there are still some difficulties in properly modeling dislocation dynamics while considering dislocation climb at high temperatures. Tsukada et al. [11,12] developed a phase-field model that simultaneously models both morphological change of the γ' phase and the microstructure-dependent heterogeneous creep of the γ phase. In their calculation of creep in the γ phase, the dislocation dynamics were not considered explicitly, but rather a macroscopic and phenomenological relationship between the strain-rate and stress at high temperatures was assumed. Three-dimensional (3D) simulations based on their model successfully reproduced the rafting phenomenon and the macroscopic creep rate–time curve in the initial stage of the creep of CMSX-4 at 1273 K under the tensile stress of 160 MPa along the [001] direction [12]. Their model is presumed to be able to simulate the rafting rate and its dependence on the external stress condition.

In this study, the rafting phenomenon during the creep in CMSX-4 at 1273 K under the tensile stresses of 130 MPa and 100 MPa is simulated using the phase-field method. Following Tsukada et al.'s [11,12] model, inelastic strain in the γ phase is assumed to consist of the plastic strain (ε^{p}) and creep strain (ε^{c}) contributions, and the evolution of ε^{p} and ε^{c} is calculated based on the elasticity field arising from the evolving microstructure. To examine the rate of rafting, 3D simulations are performed considering a single γ' particle and the time to rafting is defined from the simulated macroscopic creep response when rafting occurs. The simulation results for the macroscopic creep rate–time curve are compared to experimental data [21] in order to confirm the validity of the simulation model, and the effect of the changes in the magnitude of external stress on the rafting rate is examined. Furthermore, external stress is removed at an arbitrary strain in the simulation at 1273 K in order to elucidate whether the rafting occurs during the subsequent heat treatment without external stress. Using the phase-field method, we explore the value of $\varepsilon_{\mathrm{th}}$ under the stress in the 100–160 MPa range, the

dependence of ε_{th} on the external stress magnitude, and the effect of the removal of external stress on the rafting kinetics.

2. Calculation method

2.1 Phase-field model

The phase-field model developed by Tsukada et al. [11,12] is adopted in this study. The local volume fraction of the γ' phase $f(\mathbf{r}, t)$ and the structural order parameters $\varphi_i(\mathbf{r}, t)$ ($i = 1,2,3,4$) are employed as the field variables that describe the (γ + γ') two-phase microstructure, with i specifying four different ordered domains of the γ' phase. All field variables are functions of space ($\mathbf{r}$) and time (t). The temporal evolution of the field variables is given by the Cahn–Hilliard and Allen–Cahn equations as follows [22]:

$$\frac{\partial f(\mathbf{r}, t)}{\partial t} = M_f \nabla^2 \frac{\delta G}{\delta f(\mathbf{r}, t)}, \tag{1}$$

$$\frac{\partial \varphi_i(\mathbf{r}, t)}{\partial t} = - L \frac{\delta G}{\delta \varphi_i(\mathbf{r}, t)}, i = 1,2,3,4, \tag{2}$$

where G is the total free energy, M_f is the γ/γ' diffusion mobility [12], and L is the structural relaxation coefficient. The total free energy G is a functional of the field variables given by [11,12,23]

$$G = \int_{\mathbf{r}} \begin{bmatrix} \{1 - h(\varphi_i)\} G^{(\gamma)}(f^{(\gamma)}) + h(\varphi_i) G^{(\gamma')}(f^{(\gamma')}) \\ + wg(\varphi_i) + \frac{\kappa_\varphi}{2} \Sigma_{i=1}^4 (\nabla \varphi_i)^2 \end{bmatrix} d\mathbf{r} + E_{el},$$

$$h(\varphi_i) = \Sigma_{i=1}^4 [\varphi_i^3 (10 - 15\varphi_i + 6\varphi_i^2)],$$

$$g(\varphi_i) = \sum_{i=1}^{4} \left[\varphi_i^2 (1 - \varphi_i)^2 \right] + \alpha \sum_{i=1}^{4} \sum_{j \neq i}^{4} \varphi_i^2 \varphi_j^2 .$$

Here $G^{(\gamma)}$ and $G^{(\gamma')}$ are the Gibbs energy densities of γ and γ' phases, and are assumed to be given by $G^{(\gamma)} = W^{(\gamma)} f^2$ and $G^{(\gamma')} = W^{(\gamma')}(1-f)^2$, respectively, and $W^{(\gamma)}$ and $W^{(\gamma')}$ are energy coefficients that can be estimated using the thermodynamic parameters of the phase diagram. Following Kim et al.'s [24] model, the γ/γ' interface region is regarded as a mixture of the γ and γ' phases with different γ' volume fractions $f^{(\gamma)}$ and $f^{(\gamma')}$, with equal chemical potentials. w is the double-well potential height, κ_φ is the gradient energy coefficient, and E_{el} is the elastic strain energy. w and κ_φ are related to both the γ/γ' interface energy (γ_s) and the interface thickness (2λ) as $\gamma_s = \sqrt{w \kappa_\varphi}/3\sqrt{2}$ and $2\lambda = \alpha \sqrt{2\kappa_\varphi/w}$; α depends on the definition of 2λ and is set to be $\alpha = 2$ [24]. E_{el} is given by [25,26]

$$E_{\mathrm{el}} = \int_{\mathbf{r}} \left[\begin{array}{c} \frac{1}{2} C_{ijkl}(\mathbf{r}, t) \left\{ \varepsilon_{ij}(\mathbf{r}, t) - \varepsilon_{ij}^0(\mathbf{r}, t) \right\} \left\{ \varepsilon_{kl}(\mathbf{r}, t) - \varepsilon_{kl}^0(\mathbf{r}, t) \right\} \\ - \sigma_{ij}^{\mathrm{appl}} \bar{\varepsilon}_{ij} \end{array} \right] d\mathbf{r} . \qquad (3)$$

The elastic constant C_{ijkl} is assumed to be given by $C_{ijkl} = \left\{ 1 - h(\varphi_i) \right\} C_{ijkl}^{(\gamma)} + h(\varphi_i) C_{ijkl}^{(\gamma')}$, where $C_{ijkl}^{(\gamma)}$ and $C_{ijkl}^{(\gamma')}$ represent the elastic constants of the γ and γ' phases, respectively. ε_{ij} is the total strain, ε_{ij}^0 is the eigenstrain, $\sigma_{ij}^{\mathrm{appl}}$ is the applied external stress, and $\bar{\varepsilon}_{ij}$ is the uniform macroscopic strain defined as $\bar{\varepsilon}_{ij} \equiv \int_{\mathbf{r}} \varepsilon_{ij} d\mathbf{r}/V$, where V is the system volume. Note that the Einstein summation convention is applied in Eq. (3). The body is allowed to relax at fixed $\sigma_{ij}^{\mathrm{appl}}$ (stress-controlled boundary condition) and $\bar{\varepsilon}_{ij}$ is determined by minimizing E_{el} with respect to $\bar{\varepsilon}_{ij}$. To calculate ε_{ij}, the mechanical equilibrium equation ($\partial \sigma_{ij}/\partial r_j = 0$, $\sigma_{ij} = C_{ijkl}(\mathbf{r}, t) \left\{ \varepsilon_{kl}(\mathbf{r}, t) - \varepsilon_{kl}^0(\mathbf{r}, t) \right\}$) is solved in Fourier space by using an iterative perturbation approach [27,28]. ε_{ij}^0 is defined by [11,12]

$$\varepsilon_{ij}^0(\mathbf{r}, t) = \varepsilon_0 \delta_{ij} h(\varphi_i) + \varepsilon_{ij}^{\mathrm{p}}(\mathbf{r}, t) + \varepsilon_{ij}^{\mathrm{c}}(\mathbf{r}, t),$$

where δ_{ij} is the Kronecker delta function and ε_0 is the lattice misfit calculated from the lattice parameter of each phase as $\varepsilon_0 = (a^{(\gamma')} - a^{(\gamma)})/a^{(\gamma)}$. $\varepsilon_{ij}^{\mathrm{p}}$ and $\varepsilon_{ij}^{\mathrm{c}}$ are the plastic strain and creep strain, respectively. The evolution of $\varepsilon_{ij}^{\mathrm{p}}$ is calculated by [29]

$$\frac{\partial \varepsilon_{ij}^{\mathrm{p}}(\mathbf{r}_{\mathrm{p}}, t)}{\partial t} = - K_{ijkl} \frac{\delta E_{\mathrm{shear}}}{\delta \varepsilon_{kl}^{\mathrm{p}}(\mathbf{r}_{\mathrm{p}}, t)}. \tag{4}$$

Here K_{ijkl} is the kinetic coefficient and E_{shear} is the shear strain energy. For simplicity, K_{ijkl} is assumed to be given by $K_{ijkl} = K\delta_{ik}\delta_{jl}$. Eq. (4) is iteratively solved at $\mathbf{r}_{\mathrm{p}}$, where the von Mises yield criterion is exceeded, until the equivalent stress ($\overline{\sigma}$) becomes smaller than the yield stress of the γ phase (σ_{y}) in the entire γ-phase region. E_{shear} is given by

$$E_{\mathrm{shear}} = \int_{\mathbf{r}} \left[\frac{1}{2} C_{ijkl}(\mathbf{r}, t)\{e_{ij}(\mathbf{r}, t) - e_{ij}^0(\mathbf{r}, t)\}\{e_{kl}(\mathbf{r}, t) - e_{kl}^0(\mathbf{r}, t)\} - s_{ij}^{\mathrm{appl}}\overline{e}_{ij} \right] d\mathbf{r},$$

where e_{ij} and s_{ij} correspond to the deviatoric strain and stress, respectively. The evolution of $\varepsilon_{ij}^{\mathrm{c}}$ is calculated on the basis of the von Mises creep theory according to [11,12,30]

$$\frac{\partial \varepsilon_{ij}^{\mathrm{c}}(\mathbf{r}, t)}{\partial t} = \frac{3}{2} C \overline{\sigma}^4(\mathbf{r}, t) s_{ij}(\mathbf{r}, t). \tag{5}$$

Here C is the creep coefficient and $\overline{\sigma}$ is the equivalent stress, which is given by

$$\overline{\sigma} = \sqrt{\frac{1}{2}\{(\sigma_{11} - \sigma_{22})^2 + (\sigma_{22} - \sigma_{33})^2 + (\sigma_{33} - \sigma_{11})^2\} + 3(\sigma_{12}^2 + \sigma_{23}^2 + \sigma_{31}^2)}.$$

The region where $h(\varphi_i) < 0.5$ is regarded as the γ phase, and $\varepsilon_{ij}^{\mathrm{p}}$ and $\varepsilon_{ij}^{\mathrm{c}}$ are assumed to be confined to the γ phase. Eqs. (4) and (5) are solved only in the γ phase, and $\varepsilon_{ij}^{\mathrm{p}}$ and $\varepsilon_{ij}^{\mathrm{c}}$ are assumed to not be inherited into the γ' phase when the morphology of the γ' phase changes.

2.2 Simulation conditions

We use $32 \times 32 \times 32$ computational grids for 3D simulations. The simulated system size is $256 \times 256 \times 256$ nm^3 and the periodic boundary conditions are assumed in all three dimensions. Eqs. (1), (2), (4), and (5) are solved using the finite difference method. In numerical analysis, all physical parameters are reduced to dimensionless quantities using the scaling factors of RT for energy, l_0 for length, and $(M_f RT/l_0^2)^{-1}$ for time, where R is the gas constant, T is the absolute temperature, and l_0 is the unit grid size. To maintain numerical accuracy and stability, the unit time step Δt^* is selected as $\Delta t^* = 0.2$, where the superscript $*$ denotes a dimensionless quantity. The parameters used in the simulations are summarized in Table 1 [12]. The value of M_f is estimated using the database of multicomponent atomic diffusion mobility values [12,31]. The $W^{(\gamma)}$ and $W^{(\gamma')}$ values are estimated from the Gibbs energy curve of each phase at 1273 K calculated using the thermodynamic parameters of the phase diagram of the Ni–Al system [32]. The parameters w and κ_φ are fitted to the γ/γ' interface energy $\gamma_s = 0.0142$ J m^{-2} [33]. The elastic constants and lattice misfit of CMSX-4 at 1273 K [34,35] are used and the 0.5% proof stress for the single-crystal γ-phase alloy [36] is employed as the yield stress. The creep coefficient C at 1273 K has been determined such that the simulation reproduces the macroscopic creep rate–time curve of CMSX-4 at 1273 K under a tensile stress of 160 MPa along the [001] direction [12]. Due to the lack of experimental data, the structural relaxation coefficient L in Eq. (2) is not well-determined and is set to be sufficiently large to ensure that the microstructure evolution is diffusion controlled. The initial microstructure of the simulation is shown in Fig. 1; the γ phase is transparent and the γ/γ' interface is shown in white. The

cuboidal γ' phase with an edge length of approximately 200 nm is placed at the center of the computational cell. Since a single γ' particle is considered in the simulation, φ_1 is assigned to the γ' particle and $\varphi_2–\varphi_4$ are not used in this study.

3. Results

3.1 Rafting under the external tensile stress

Figure 2(a) shows the simulation results for microstructure evolution during creep at 1273 K under the external tensile stress of 130 MPa along the [001] direction. In the figure, the γ'-phase interior is shown in red. The figure shows that the morphology of the γ' phase gradually changes, the γ' phase connects with the neighboring γ' particles aligned along the [100] and [010] directions, and the (001) lamellar structure (rafted structure) is formed. Figure 2(b) shows the 3D contours of the equivalent strain rate ($\dot{\bar{\varepsilon}}^p + \dot{\bar{\varepsilon}}^c$). Here the equivalent strain is given by

$$
\bar{\varepsilon}^p = \sqrt{\frac{2}{3}\varepsilon_{ij}^p \varepsilon_{ij}^p},
$$
$$
\bar{\varepsilon}^c = \sqrt{\frac{2}{3}\varepsilon_{ij}^c \varepsilon_{ij}^c}.
$$

When the rafting occurs ($t = 25.8$ h), the strain rate temporarily increases in the γ-phase region. In particular, the strain rate is high near the region where the γ' phase shows a negative curvature, as indicated by the arrows in Figs. 2(a) and 2(b). No morphological changes of the γ' phase are observed in the simulation after the formation of the (001) rafted structure. Figure 3 shows the simulation results at 1273 K under the external tensile stress of 100 MPa along the [001] direction. The results shown in Fig. 3 are similar to those shown in Fig. 2: the (001) rafted structure is formed and a temporary increase in the strain rate is observed in the γ-phase region when rafting occurs (see the region shown by the arrows in Figs. 3(a) and 3(b)). However, the

time to rafting differs between the simulations for the 130 MPa and 100 MPa stresses (compare Figs. 2 and 3). Rafting occurs at $t\sim 25$ h under the 130 MPa stress, while it occurs at $t\sim 131$ h under the 100 MPa stress. Thus, the time to rafting increases with decreasing magnitude of the external tensile stress.

Figures 4(a) and 4(b) show the macroscopic creep rate–time curves of CMSX-4 at 1273 K under the tensile stresses of 130 MPa and 100 MPa, respectively. Solid and open symbols represent the simulation results and experimental data [21], respectively. In the simulation, the macroscopic strain along the [001] direction is calculated by

$$\varepsilon = \frac{1}{V}\int_{\mathbf{r}}\{\varepsilon_{33}^{\mathrm{p}}(\mathbf{r}, t) + \varepsilon_{33}^{\mathrm{c}}(\mathbf{r}, t)\}d\mathbf{r},$$

where V is the system volume. Figure 4 shows that the simulation results reproduce the experimental data in the initial stage of transient creep. In the simulation, a sharp and temporary increase in the creep rate is observed, as indicated by the arrows in Figs. 4(a) and 4(b). This is attributed to γ' rafting. As shown in Figs. 2 and 3, the creep rate temporarily increases in the γ-phase region when rafting occurs, influencing the macroscopic creep response and giving rise to a "spike" in the creep rate–time curve. Experimentally, an "S-shaped" creep strain–time curve (temporary increase in creep rate) assumed to be related to rafting has been observed in the initial stage of the high-temperature creep of a nickel-based superalloy [37]. In our simulations, the creep rate decreases monotonically after the formation of the rafted structure and the acceleration of the creep rate in the later stage of creep is not reproduced; the simulation of such acceleration is beyond the scope of this paper. In the experiments performed by Miura et al. [21], the rafting progresses inhomogeneously in the microstructure, and hence, the cuboidal and rafted γ' phases coexist; this blurs the temporary increase in the macroscopic creep rate arising from the rafting and makes it difficult to define the time to rafting. In our simulation considering a single γ' particle, the time when a spike (a sharp increase in creep rate) is observed

in the macroscopic creep rate–time curve is defined as the time to rafting.

3.2 Threshold value of strain for inducing rafting

The threshold value of macroscopic strain for inducing rafting, ε_{th}, is examined using the simulations. In a creep simulation, the applied external stress is removed at an arbitrary strain and the system is examined for the occurrence of rafting in the subsequent heat treatment without external stress. Figure 5(a) shows the microstructure at $\varepsilon = 0.14\%$ ($t = 57.0$ h) during creep at 1273 K under the tensile stress of 100 MPa along the [001] direction. Figures 5(b) and 5(c) show the 3D contours of equivalent plastic strain ($\bar{\varepsilon}^p$) and equivalent creep strain ($\bar{\varepsilon}^c$) at $\varepsilon = 0.14\%$, respectively. The amount of plastic strain is preferentially large in the (001) γ phase (horizontal γ channels). By contrast, the creep strain is localized near the γ/γ' interface in the horizontal γ channels and the amount of creep strain is small in the vertical γ channels. Figure 6(a) shows the microstructure at $\varepsilon = 0.14\%$ ($t = 57.0$ h) and $\varepsilon = 0.16\%$ ($t = 103.2$ h) during creep at 1273 K under the tensile stress of 100 MPa along the [001] direction. At $\varepsilon = 0.14\%$ and $\varepsilon = 0.16\%$, the rafting does not occur and the γ' phase is cuboidal. Figure 5(b) shows the 3D contours of the equivalent strain ($\bar{\varepsilon}^p + \bar{\varepsilon}^c$) at $\varepsilon = 0.14\%$ and $\varepsilon = 0.16\%$. It is seen that there is little difference in the strain distribution between $\varepsilon = 0.14\%$ and $\varepsilon = 0.16\%$. Figure 7 shows the microstructure evolution at 1273 K when the external stress of 100 MPa along the [001] direction is removed. For the systems presented in Figs. 7(a) and 7(b), the external stress is removed when the macroscopic strain reaches $\varepsilon = 0.14\%$ ($t = 57.0$ h) and $\varepsilon = 0.16\%$ ($t = 103.2$ h), respectively. In Fig. 7(a), the γ' phase remains cuboidal and the rafting does not occur. On the other hand, in Fig. 7(b), the γ' phase evolves to form the (001) rafted structure even without external stress. Figure 7 shows that $\varepsilon_{th} = 0.14\%–0.16\%$ when an external stress of 100 MPa is removed at 1273 K. Similar simulations are performed at 1273 K when an external stress of 130 MPa or 160 MPa is removed at arbitrary strains with $\varepsilon_{th} = 0.14\%–0.16\%$

for the removal of stress of 160 MPa and $\varepsilon_{th} = 0.12\%-0.14\%$ for the removal of stress of 130 MPa. Although this numerical trial-and-error search is not exhaustive and the precise value of ε_{th} has not yet been obtained, it is presumed that the dependence of ε_{th} on the magnitude of the external tensile stress is small at 1273 K in the 100–160 MPa stress range.

The rafting kinetics with and without external stress when the macroscopic strain exceeds ε_{th} are examined in detail. Figure 8 shows the simulation results for the time to rafting after $\varepsilon = 0.16\%$ is reached. In the stress range of 100–160 MPa, the γ' phase is cuboidal at $\varepsilon = 0.16\%$ and rafting occurs during the subsequent heat treatment with and without external stress. Figure 8 shows that when external stress is continuously applied (see the open symbols in Fig. 8), the time to rafting after reaching $\varepsilon = 0.16\%$ increases with decreasing magnitude of the applied external stress. On the other hand, when external stress is removed at $\varepsilon = 0.16\%$ (see the solid symbols in Fig. 8), the time to rafting after the removal of external stress is $t{\sim}2.5$ h, which is almost independent of the magnitude of the applied external stress. Furthermore, Fig. 8 shows that rafting is accelerated by the removal of external stress and the degree of acceleration increases with decreasing applied external stress magnitude.

4. Discussion

All simulation parameters (Table 1) are assumed to be independent of the applied external stress. Hence, the microstructure evolution at 1273 K has been simulated by only changing the magnitude of the external tensile stress along the [001] direction. Not only the rafting phenomenon during creep but also the macroscopic creep rate–time curve has been successfully simulated under the 130 MPa and 100 MPa stresses, as shown in Fig. 4. However, the acceleration of the creep rate in the later creep stage is not reproduced by the simulation. Experimentally, it has been observed [21,38,39] that following the occurrence of rafting, the γ-channel thickness increases as a result of coalescence of the rafted structures and a close

relationship exists between the creep rate during the accelerating creep stage and the γ-channel thickness [21]. Since we aim to reveal the rate of rafting in this study, our simulation considers a single γ' phase; therefore, the coalescence of the rafted structure and the resultant acceleration of the creep rate in the later stage of creep is beyond the scope of this paper, and is not simulated. Large-scale simulation considering several γ' particles may reproduce not only the rafting phenomenon but also the coalescence of the rafted structure, and may provide new insight into the onset of acceleration of the creep rate.

In our previous simulations at 1273 K [12], the rafting was observed at $t \sim 8$ h under a stress of 160 MPa. Combined with the simulation results shown in Figs. 2 and 3, these results show that the time to rafting increases with decreasing magnitude of the applied external stress. This tendency was confirmed by Miura et al. in their experimental study [21], where the microstructure of the creep-interrupted specimens was examined in detail in various external tensile stress conditions. Some phase-field simulation studies [5,7] have revealed that plasticity in the γ phase plays a dominant role in rafting. Hence, a smaller magnitude of the applied external stress leads to a longer time required for the introduction of a sufficient γ-phase plasticity for inducing rafting. In Section 3.2, the threshold strain required for rafting is simulated as $\varepsilon_{th} = 0.12\%$–$0.16\%$ at 1273 K in the stress range of 100–160 MPa. Note that the simulated value of ε_{th} is close to the value determined experimentally at 1223 K under the stress of 185 MPa ($\varepsilon_{th} = 0.10 \pm 0.03\%$) [16].

Matan et al. [16] suggested that the plasticity in the horizontal γ channels ((001) channels) causes a loss of perfect coherency and reduction in the elastic misfit strains, enabling rafting to occur at a reasonable speed. They attempted to determine the relationship between ε_{th} and the lattice misfit ε_0 based on the following assumptions. First, it was assumed that mobile dislocations are confined to the horizontal γ channels and relieve the misfit strain at the γ/γ' interface. Second, all generated dislocations were assumed to remain in the structure without any climb- and annihilation-driven reduction in their number. They showed that, under

these assumptions, ε_{th} can be estimated by

$$\varepsilon_{th} = 2\varepsilon_0\left(1 - f_{\gamma'}^{1/3}\right), \tag{6}$$

where $f_{\gamma'}$ is the volume fraction of the γ' phase. Using the simulation conditions in this study, ε_{th} can be estimated from Eq. (6) as $\varepsilon_{th} = 0.086\%$. This is nearly one-half of the simulated value of ε_{th} reported in Section 3.2. This discrepancy may be attributed to the fact that even though the inelastic strain (plastic strain and creep strain) prefers the horizontal γ channels in the simulations, a non-negligible inelastic strain occurs in the vertical γ channels as well (Fig. 6). A similar result was obtained by Zhou et al. in their phase-field simulation study [10]. This result disagrees with Matan et al.'s [16] assumption that there is no dislocation activity in the vertical γ channels. In the presence of an inelastic strain in the vertical γ channels, the ε_{th} value sufficient for relieving the lattice misfit in the horizontal channels should be larger than that estimated from Eq. (6). To predict the value of ε_{th} and its dependence on material parameters, calculating the equilibrium shapes of interacting inclusions in an elastically inhomogeneous system may be useful [40]. However, incorporating the effect of inelastic strain of the matrix into the calculation appears to be a challenging problem.

There are two contributions to rafting: elastic inhomogeneity (modulus mismatch between the γ and γ' phases) and γ-channel plasticity. Zhou et al. [7] showed that while γ-channel plasticity plays a dominant role in rafting, the contribution of elastic inhomogeneity to rafting kinetics is not negligible. During the first several hours of creep after the application of external stress, the driving force for rafting due to elastic inhomogeneity is significant [7]. Therefore, it may be assumed that the existence of external stress generally increases rafting kinetics. However, this does not necessarily apply to the case where macroscopic strain exceeds ε_{th}. As shown in Fig. 8, our simulation results suggest that the removal of external stress at $\varepsilon = 0.16\%$ increases the rate of rafting. Matan et al. [16] reported that the removal of external

14

stress has a negligible influence on the rafting kinetics in their experiments at 1223 K under the stress of 185 MPa. A similar result can also be seen in our simulations with and without an applied external stress of 160 MPa (Fig. 8). Figure 8 shows that the acceleration of rafting due to the removal of external stress can be significant at 1273 K under external stresses lower than 160 MPa.

Figures 9(a) and 9(b) show the simulation results for the 3D contours of the equivalent strain ($\bar{\varepsilon}^{\mathrm{p}} + \bar{\varepsilon}^{\mathrm{c}}$) and equivalent stress ($\bar{\sigma}$), respectively, when the external stress along the [001] direction is removed at $\varepsilon = 0.16\%$. The simulation results are shown for the external stresses of 160, 130, and 100 MPa. Figure 9(a) shows that the strain is accumulated preferentially at the horizontal γ channels. Furthermore, Fig. 9(b) shows that the residual stress occurs in the γ phase and is preferentially high in the vertical γ channels. In our simulation, even after the external stress is removed, the residual stress induces inelastic strain evolution in the γ phase. Figure 10 shows the simulation results of the change in macroscopic strain along the [001] direction ε during the heat treatment at 1273 K after the removal of external stress. We see that ε decreases with time, indicating that the compressive stress along the [001] direction is the major component of the residual stress shown in Fig. 9(b). If the energetic stability of the (001) rafted structure is considered using the concept of "effective eigenstrain" comprising the lattice misfit and inelastic strain via creep deformation [6,41], the driving force for rafting decreases with decreasing ε. Hence, the simulation results shown in Fig. 10 imply that the driving force for rafting decreases during the heat treatment after the removal of external stress. However, ε variation is small and its effect on rafting kinetics is assumed to be negligible. Actually, as shown in Fig. 8, rafting is accelerated by the removal of external stress and the time to rafting after the removal of external stress is $t{\sim}2.5$ h, independent of the magnitude of the applied external stress.

To explain the acceleration of rafting due to the removal of external stress, the elastic strain energy of the (γ + γ') microstructure is calculated using Eq. (3) according to the

following procedure. We use $128 \times 128 \times 128$ computational grids for the calculation, and place a single γ' phase with dimensions $a \times a \times c$ at the center of the computational cell. Values of a and c are multiples of the grid spacing and are varied such that the volume fraction of the γ' phase is approximately equal (0.536 ± 0.002). The elastic constants and lattice misfit shown in Table 1 are used. For simplicity, a homogeneous inelastic strain of 0.345% along the [001] direction is assumed in the γ phase; this corresponds to the macroscopic strain of 0.16% along the [001] direction. The external tensile stress is applied along the [001] direction. Before the calculation of E_{el}, the γ/γ' interface is smoothened by solving Eqs. (1) and (2) for $t^* = 200$ without considering E_{el}. Figure 11 shows the calculated elastic strain energy as a function of the $1 - c/a$ shape factor. The figure shows that starting from $c/a = 1$, the elastic strain energy decreases with decreasing c/a. This result shows that a morphological change from the cuboidal γ' phase ($c/a = 1$) to the (001) rafted structure ($c/a < 1$) is favorable from the viewpoint of elastic strain energy relaxation. Figure 12 shows the gradient of the elastic strain energy given by $dE_{\text{el}}/d(1 - c/a)$ and calculated based on the data shown in Fig. 11. In Fig. 12, the driving force for rafting under different stress conditions can be compared at each value of c/a; a larger absolute value of $dE_{\text{el}}/d(1 - c/a)$ gives rise to a larger driving force for rafting. At most c/a values, the driving force for rafting under external stress is larger than that without external stress. However, the driving force for rafting is increased by the removal of the external stress at $c/a \sim 0.90$. In other words, rafting is accelerated by the removal of external stress if c/a ~0.90 when the macroscopic strain reaches $\varepsilon = 0.16\%$ during creep at 1273 K. Our simulation results show that, even before the macroscopic strain exceeds ε_{th}, the shape of the γ' phase changes slightly and the c/a value decreases from 1; the shape factor of the γ' phase is $c/a \sim 0.85$ at $\varepsilon = 0.16$ in the stress range of 100–160 MPa. Note that this c/a value is close to $c/a \sim 0.90$, which has been predicted from the simplified calculation of the elastic strain energy shown in Figs. 11 and 12. We presume that the acceleration of rafting by the removal of external stress cannot be observed under stresses higher than 160 MPa. If the external stress is high, the creep

strain would increase so rapidly that the shape of the γ' phase would still remain cuboidal (c/a $\sim$1) at $\varepsilon = 0.16$; hence, the rafting would not be accelerated by the removal of external stress.

In this study, we focus on the effect of external stress on rafting kinetics. However, the atomic diffusion mobility of constituent elements also has a significant effect on rafting kinetics. In their phase-field simulation study, Mushongera et al. [14] showed that the rafting process is slower in CMSX-4 than in CMSX-6, and that the presence of Re, which is a slow diffusion element in CMSX-4, plays a major role in the reduction of the rafting rate. In the phase-field model employed in this study, the effect of Re diffusion has been incorporated into the γ/γ' diffusion mobility M_f in Eq. (1) by estimating the value of M_f from the multicomponent atomic diffusion mobility database [12,31]. Hence, it is possible to simulate the rafting rate with and without the slow diffusion elements such as Re, W, Ta and Mo. The simulation method shown in this study is assumed to have the ability to analyze the rafting kinetics that are influenced by the presence of slow diffusion elements, the magnitude of applied external stress, the presence of external stress when the macroscopic strain exceeds ε_{th}, and the simulation inputs such as elastic constants and lattice misfit. In the future, simulations using different external/material parameters as inputs will be necessary to elucidate the most effective parameters for controlling the rafting rate and the value of ε_{th}. The assumption of the isotropic yield criterion for calculating the evolution of plastic strain is the limitation of our model. The development of a new yield criterion that incorporates the anisotropic hardening mechanism should be important for a more accurate description of single-crystal plasticity. Moreover, the phase-field approach to modeling dislocation dynamics considering dislocation climb at high temperatures is necessary for simulating the dislocation structure during creep and its effect on the rate of rafting.

5. Conclusions

The rafting kinetics during the creep of the nickel-based single crystal superalloy CMSX-4 have been simulated at 1273 K using a phase-field model that considers both morphological change of the γ' phase and heterogeneous creep of the γ phase. The directional coarsening of the γ' phase (rafting) and the macroscopic creep rate–time curve in the initial stage of creep have been successfully simulated under the external tensile stresses of 130 MPa and 100 MPa along the [001] direction. It has been shown that the time to rafting increases with decreasing magnitude of the applied external stress. Furthermore, the simulations where external stress is removed at arbitrary strains show that the threshold value of the macroscopic strain for inducing rafting is $\varepsilon_{th} = 0.12\%$–$0.16\%$ at 1273 K in the stress range of 100–160 MPa. The simulation results show that rafting is accelerated by the removal of external stress when the macroscopic strain exceeds ε_{th}, and that the degree of the acceleration is significant under an external stresses lower than 160 MPa. Using a simplified calculation of the elastic strain energy of the (γ + γ') microstructure, it has been shown that the driving force for rafting can be increased by the removal of external stress when the macroscopic strain exceeds ε_{th}. The simulation method employed in this study is useful for analyzing the rate of rafting and for accumulating fundamental knowledge on rafting kinetics during the high-temperature creep in nickel-based superalloys.

Acknowledgments

References

[1]   R.C. Reed, The superalloys fundamentals and applications, Cambridge University Press, New York, 2006.

[2]   T.M. Pollock, A.S. Argon, Directional coarsening in nickel-base single crystals with high volume fractions of coherent precipitates, Acta Metall. Mater. 42 (1994) 1859−1874.

[3]   D.Y. Liu, L.Q. Chen, Computer simulation of morphological evolution and rafting of γ′ particles in Ni-based superalloys under applied stresses, Scr. Mater. 37 (1997) 1271−1277.

[4]   M.P. Gururajan, T.A. Abinandanan, Phase field study of precipitate rafting under a uniaxial stress, Acta Mater. 55 (2007) 5015−5026.

[5]   N. Zhou, C. Shen, M.J. Mills, Y. Wang, Phase field modeling of channel dislocation activity and γ′ rafting in single crystal Ni−Al, Acta Mater. 55 (2007) 5369−5381.

[6]   Y. Tsukada, Y. Murata, T. Koyama, M. Morinaga, Phase-field simulation on the formation and collapse processes of the rafted structure in Ni-based superalloys, Mater. Trans. 49 (2008) 484−488.

[7]   N. Zhou, C. Shen, M.J. Mills, Y. Wang, Contribution from elastic inhomogeneity and from plasticity to γ′ rafting in single-crystal Ni−Al, Acta Mater. 56 (2008) 6156−6173.

[8]   N. Zhou, C. Shen, P.M. Sarosi, M.J. Mills, T. Pollock, Y. Wang, γ′ rafting in single crystal blade alloys: a simulation study, Mater. Sci. Technol. 25 (2009) 205−212.

[9]   A. Gaubert, Y. Le Bouar, A. Finel, Coupling phase field and viscoplasticity to study rafting in Ni-based superalloys, Philos. Mag. 90 (2010) 375−404.

[10] N. Zhou, C. Shen, M. Mills, Y. Wang, Large-scale three-dimensional phase field simulation of γ′-rafting and creep deformation, Philos. Mag. 90 (2010) 405−436.

[11] Y. Tsukada, Y. Murata, T. Koyama, N. Miura, Y. Kondo, Creep deformation and rafting

in nickel-based superalloys simulated by the phase-field method using classical flow and creep theories, Acta Mater. 59 (2011) 6378–6386.

[12] Y. Tsukada, T. Koyama, Y. Murata, N. Miura, Y. Kondo, Estimation of γ/γ' diffusion mobility and three-dimensional phase-field simulation of rafting in a commercial nickel-based superalloy, Comput. Mater. Sci. 83 (2014) 371–374.

[13] T. Tanimoto, Md. Moniruzzaman, Y. Murata, N. Miura, Y. Kondo, Y. Tsukada, T. Koyama, Origin of the morphological change from rafted structure to irregular shape of the γ' phase in single crystal nickel-based superalloys, Comput. Mater. Sci. 93 (2014) 56–61.

[14] L.T. Mushongera, M. Fleck, J. Kundin, Y. Wang, H. Emmerich, Effect of Re on directional γ'-coarsening in commercial single crystal Ni-based superalloys: a phase field study, Acta Mater. 93 (2015) 60–72.

[15] A. Gaubert, M. Jouiad, J. Cormier, Y. Le Bouar, J. Ghighi, Three-dimensional imaging and phase-field simulations of the microstructure evolution during creep tests of ⟨001⟩-oriented Ni-based superalloys, Acta Mater. 84 (2015) 237–255.

[16] N. Matan, D.C. Cox, C.M.F. Rae, R.C. Reed, On the kinetics of rafting in CMSX-4 superalloy single crystals, Acta Mater. 47 (1999) 2031–2045.

[17] M. Véron, Y. Bréchet, F. Louchet, Strain induced directional coarsening in Ni based superalloys, Scr. Mater. 34 (1996) 1883–1886.

[18] M.E. Kassner, Fundamentals of creep in metals and alloys, second ed., Elsevier, Amsterdam, 2009.

[19] Y.U. Wang, Y.M. Jin, A.M. Cuitiño, A.G. Khachaturyan, Nanoscale phase field microelasticity theory of dislocations: model and 3D simulations, Acta Mater. 49 (2001) 1847–1857.

[20] Y. Tsukada, Y. Kojima, T. Koyama, Y. Murata, Phase-field simulation of habit plane formation during martensitic transformation in low-carbon steels, ISIJ Int. 55 (2015)

2455–2462.

[21] N. Miura, Y. Kondo, T. Matsuo, Relation between creep rate during accelerating creep stage and γ channel thickness in single crystal nickel-based superalloy, CMSX-4, Tetsu To Hagane-J. Iron Steel Inst. Jpn. 89 (2003) 1240–1247.

[22] L.Q. Chen, Phase-field models for microstructure evolution, Annu. Rev. Mater. Res. 32 (2002) 113–140.

[23] J.Z. Zhu, T. Wang, A.J. Ardell, S.H. Zhou, Z.K. Liu, L.Q. Chen, Three-dimensional phase-field simulations of coarsening kinetics of γ' particles in binary Ni−Al alloys, Acta Mater. 52 (2004) 2837–2845.

[24] S.G. Kim, W.T. Kim, T. Suzuki, Phase-field model for binary alloys, Phys. Rev. E 60 (1999) 7186–7197.

[25] T. Mura, Micromechanics of defects in solids, second rev. ed., Martinus Nijhoff, Dordrecht, 1987.

[26] A.G. Khachaturyan, Theory of structural transformations in solids, Dover, New York, 2008.

[27] S.Y. Hu, L.Q. Chen, A phase-field model for evolving microstructure with strong elastic inhomogeneity, Acta Mater. 49 (2001) 1879–1890.

[28] Y. Tsukada, Y. Murata, T. Koyama, M. Morinaga, Phase-field simulation of the effect of elastic inhomogeneity on microstructure evolution in Ni-based superalloys, Mater. Trans. 50 (2009) 744–748.

[29] X.H. Guo, S.Q. Shi, X.Q. Ma, Elastoplastic phase field model for microstructure evolution, Appl. Phys. Lett. 87 (2005) 221910.

[30] F.K.G. Odqvist, Mathematical theory of creep and creep rupture, Oxford University Press, London, 1966.

[31] C.E. Campbell, W.J. Boettinger, U.R. Kattner, Development of a diffusion mobility database for Ni-base superalloys, Acta Mater. 50 (2002) 775–792.

[32] I. Ansara, N. Dupin, H.L. Lukas, B. Sundman, Thermodynamic assessment of the Al–Ni system, J. Alloy. Compd. 247 (1997) 20–30.

[33] A.J. Ardell, An application of the theory of particle coarsening: the γ' precipitate in Ni–Al alloys, Acta Metall. 16 (1968) 511–516.

[34] D. Siebörger, H. Knake, U. Glatzel, Temperature dependence of the elastic moduli of the nickel-base superalloy CMSX-4 and its isolated phases, Mater. Sci. Eng. A-Struct. Mater. Prop. Microstruct. Process. 298 (2001) 26–33.

[35] U. Glatzel, Neutron scattering experiments with a nickel base superalloy part II: analysis of intensity profiles, Scr. Metall. Mater. 31 (1994) 291–296.

[36] A.C. Yeh, S. Tin, Effects of Ru and Re additions on the high temperature flow stresses of Ni-base single crystal superalloys, Scr. Mater. 52 (2005) 519–524.

[37] H. Izuno, T. Yokokawa, Y. Koizumi, S. Odaka, H. Harada, A creep constructive equation of Ni-base superalloys using structural parameters, J. Japan Inst. Metals 68 (2004) 526–529.

[38] M. Kamaraj, K. Serin, M. Kolbe, G. Eggeler, Influence of stress state on the kinetics of γ-channel widening during high temperature and low stress creep of the single crystal superalloy CMSX-4, Mater. Sci. Eng. A-Struct. Mater. Prop. Microstruct. Process. 319–321 (2001) 796–799.

[39] K. Serin, G. Göbenli, G. Eggeler, On the influence of stress state, stress level and temperature on γ-channel widening in the single crystal superalloy CMSX-4, Mater. Sci. Eng. A-Struct. Mater. Prop. Microstruct. Process. 387–389 (2004) 133–137.

[40] I. Schmidt, R. Mueller, D. Gross, The effect of elastic inhomogeneity on equilibrium and stability of a two particle morphology, Mech. Mater. 30 (1998) 181–196.

[41] K. Tanaka, T. Ichitsubo, K. Kishida, H. Inui, E. Matsubara, Elastic instability condition of the raft structure during creep deformation in nickel-base superalloys, Acta Mater. 56 (2008) 3786–3790.

Captions:

Table1 Simulation parameters.

Fig. 1 Initial microstructure of simulation. γ phase is transparent and γ/γ' interface is shown in white.

Fig. 2 Simulation results of microstructure evolution during creep at 1273 K under the external tensile stress of 130 MPa along the [001] direction: (a) microstructure evolution and (b) 3D contours of equivalent strain rate ($\dot{\bar{\varepsilon}}^p + \dot{\bar{\varepsilon}}^c$).

Fig. 3 Simulation results of microstructure evolution during creep at 1273 K under the external tensile stress of 100 MPa along the [001] direction: (a) microstructure evolution and (b) 3D contours of equivalent strain rate ($\dot{\bar{\varepsilon}}^p + \dot{\bar{\varepsilon}}^c$).

Fig. 4 Macroscopic creep rate–time curves of CMSX-4 at 1273 K: (a) 130 MPa and (b) 100 MPa. Solid and open symbols represent simulation results and experimental data [21], respectively.

Fig. 5 Simulation results of (a) microstructure, (b) 3D contour of the equivalent plastic strain ($\bar{\varepsilon}^p$) and (c) 3D contour of the equivalent creep strain ($\bar{\varepsilon}^c$) at $\varepsilon = 0.14\%$ ($t = 57.0$ h) during creep at 1273 K under the tensile stress of 100 MPa along the [001] direction.

Fig. 6 Simulation results of (a) microstructure and (b) 3D contours of the equivalent strain ($\bar{\varepsilon}^p + \bar{\varepsilon}^c$) during creep at 1273 K under the tensile stress of 100 MPa along the [001] direction.

Fig. 7 Microstructure evolution at 1273 K when the external stress of 100 MPa along the [001] direction is removed. In (a) and (b), the external stress is removed when the macroscopic strain reaches $\varepsilon = 0.14\%$ ($t = 57.0$ h) and $\varepsilon = 0.16\%$ ($t = 103.2$ h), respectively.

Fig. 8 Simulation results of time to rafting after the macroscopic strain reaches $\varepsilon = 0.16\%$. Open symbols show results for the external stress along the [001] direction continuously applied after the macroscopic strain reaches $\varepsilon = 0.16\%$. Solid symbols show results for the external stress along the [001] direction removed after the macroscopic strain reaches $\varepsilon = 0.16\%$.

Fig. 9 Simulation results of (a) 3D contours of the equivalent strain ($\bar{\varepsilon}^{p} + \bar{\varepsilon}^{c}$) and (b) 3D contours of the equivalent stress ($\bar{\sigma}$) when the external stress along the [001] direction is removed at the macroscopic strain of $\varepsilon = 0.16\%$.

Fig. 10 Simulation results for change in macroscopic strain along the [001] direction during heat treatment at 1273 K after the external stress along the [001] direction is removed at the macroscopic strain of $\varepsilon = 0.16\%$.

Fig. 11 Calculation results of elastic strain energy of ($\gamma + \gamma'$) microstructure. Dimensions of the γ' phase are assumed to be $a \times a \times c$. Volume fraction of the γ' phase is 0.536 ± 0.002. Homogeneous inelastic strain of 0.345% along the [001] direction is assumed in the γ phase. External tensile stress is applied along the [001] direction.
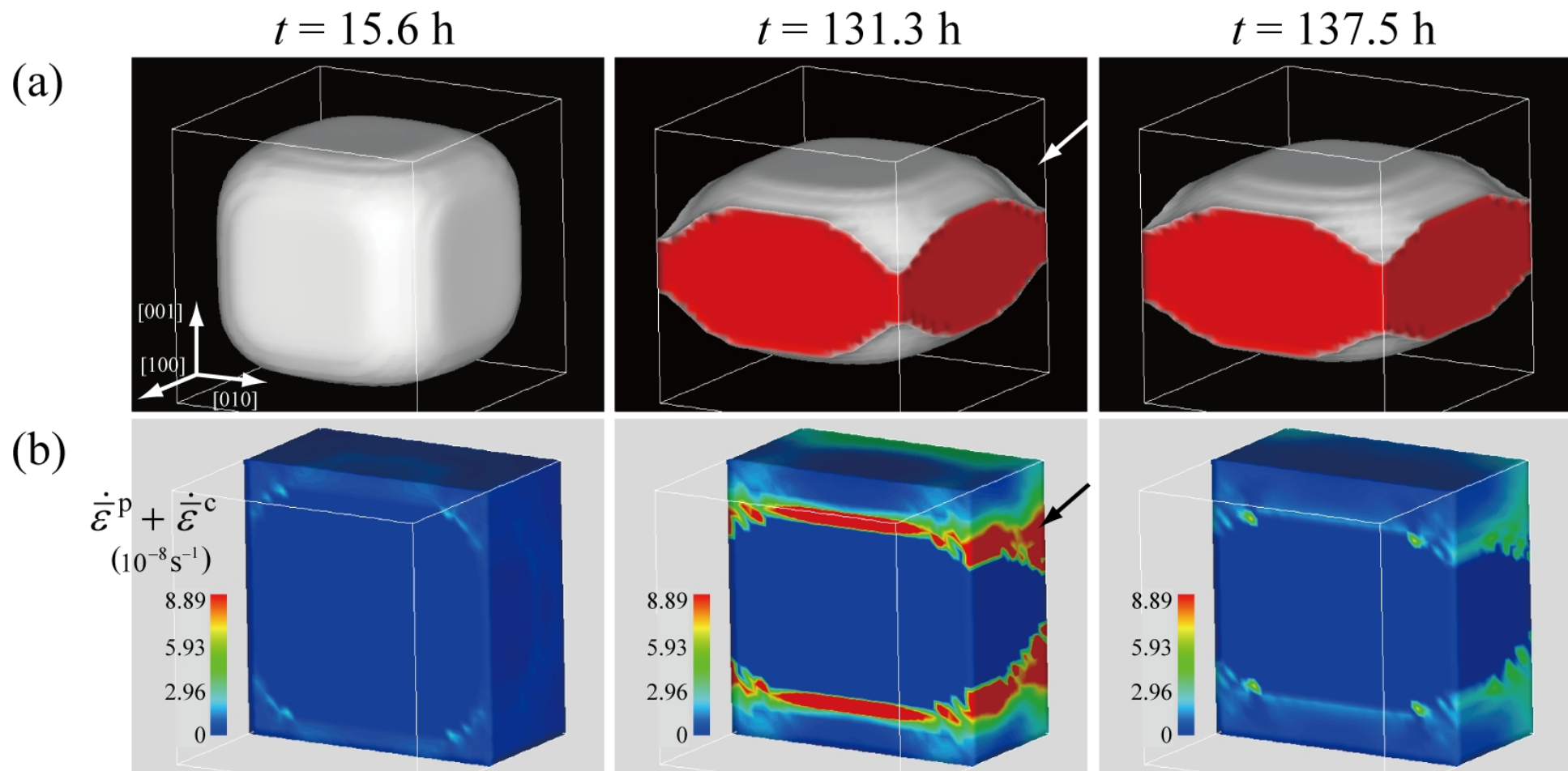
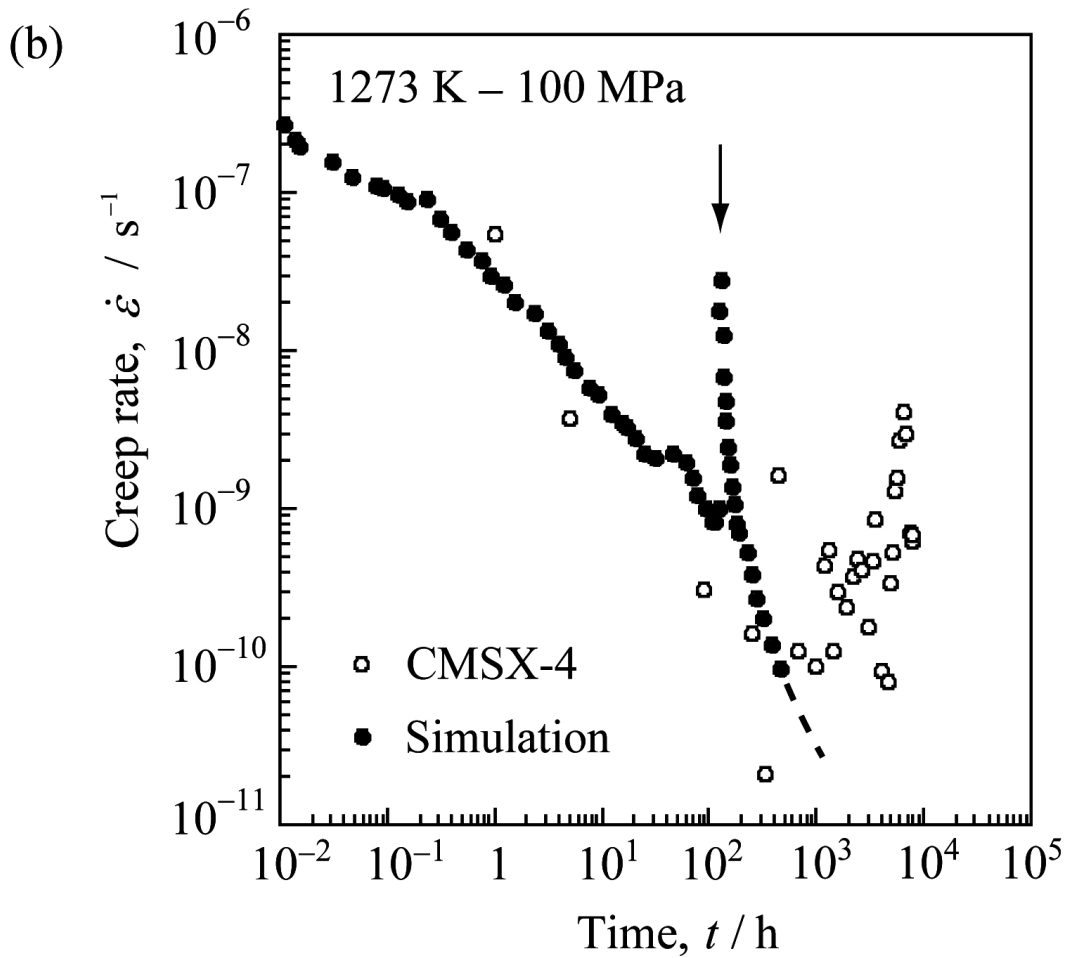Fig. 12 Calculation results of gradient of elastic strain energy. Calculations are based on the data shown in Fig. 10.
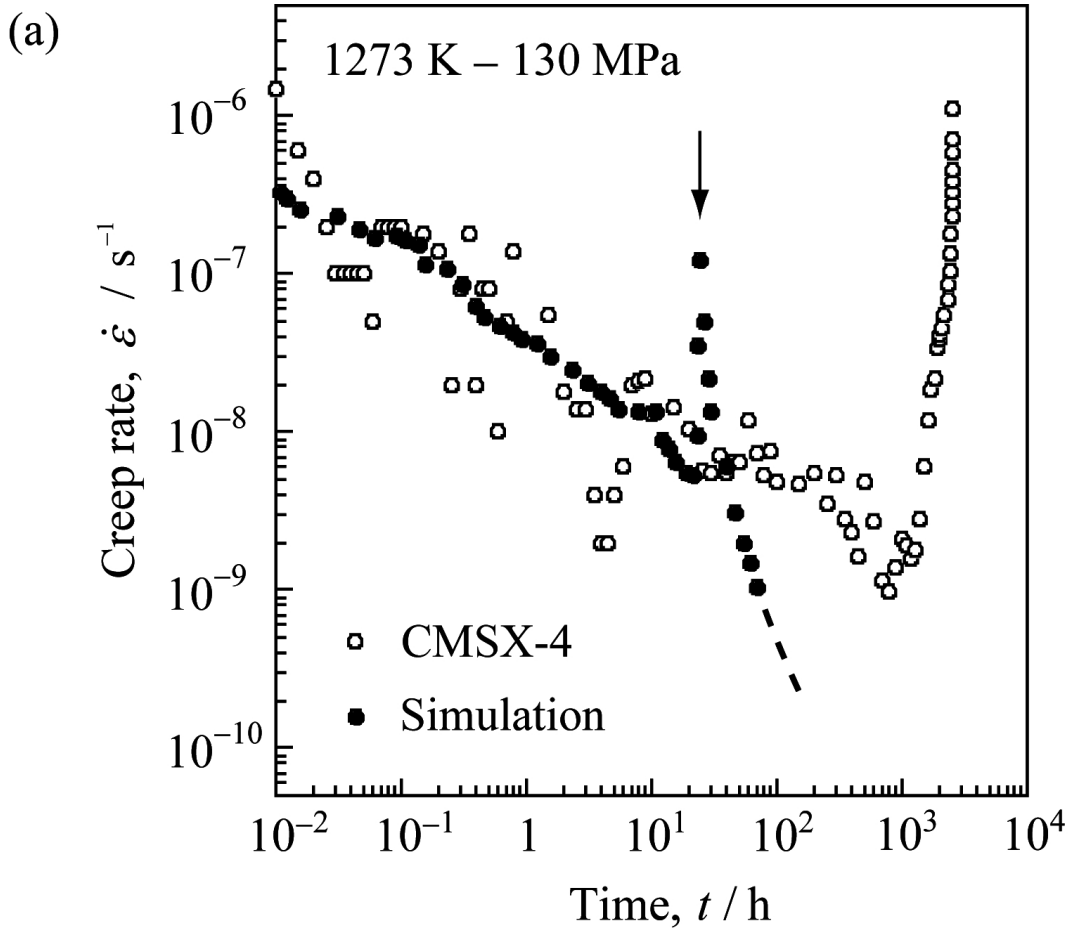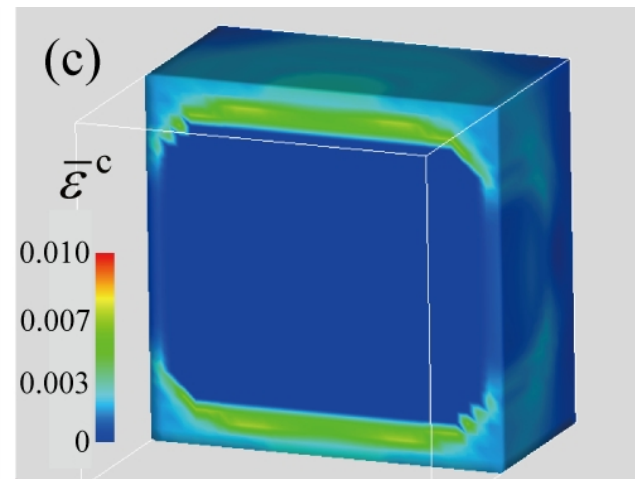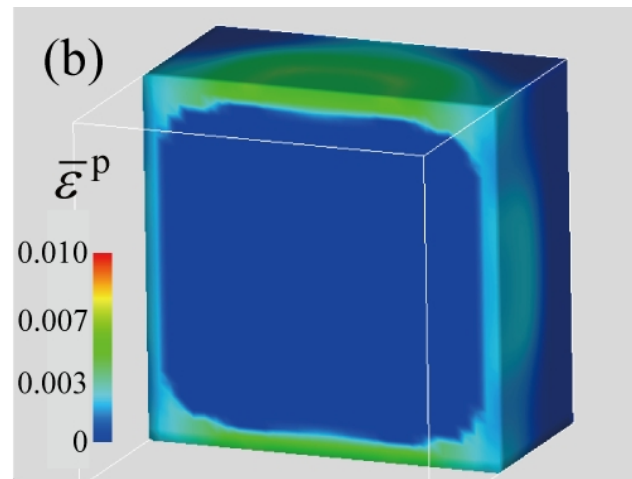
Table 1 Simulation parameters.

γ/γ' diffusion mobility, M_f (J^{-1} mol m^2 s^{-1})	2.15×10^{-20}
Gibbs energy coefficients, W (J m^{-3})	$W^{(\gamma)} = 1.29 \times 10^8$, $W^{(\gamma')} = 1.56 \times 10^8$
Double-well potential height, w (J m^{-3})	1.07×10^7
Gradient energy coefficients, κ_φ (J m^{-1})	3.41×10^{-10}
Elastic constants, C_{ijkl} (GPa)	$C_{11}^{(\gamma)} = 204.9$, $C_{12}^{(\gamma)} = 150.8$, $C_{44}^{(\gamma)} = 94.0$
	$C_{11}^{(\gamma')} = 251.6$, $C_{12}^{(\gamma')} = 194.5$, $C_{44}^{(\gamma')} = 95.0$
Lattice misfit, ε_0	-0.0023
Yield stress of the γ phase, σ_y (MPa)	120
Kinetic coefficient, K (J^{-1} mol s^{-1})	6.72×10^{-9}
Creep coefficient, C (MPa^{-5} s^{-1})	6.64×10^{-18}
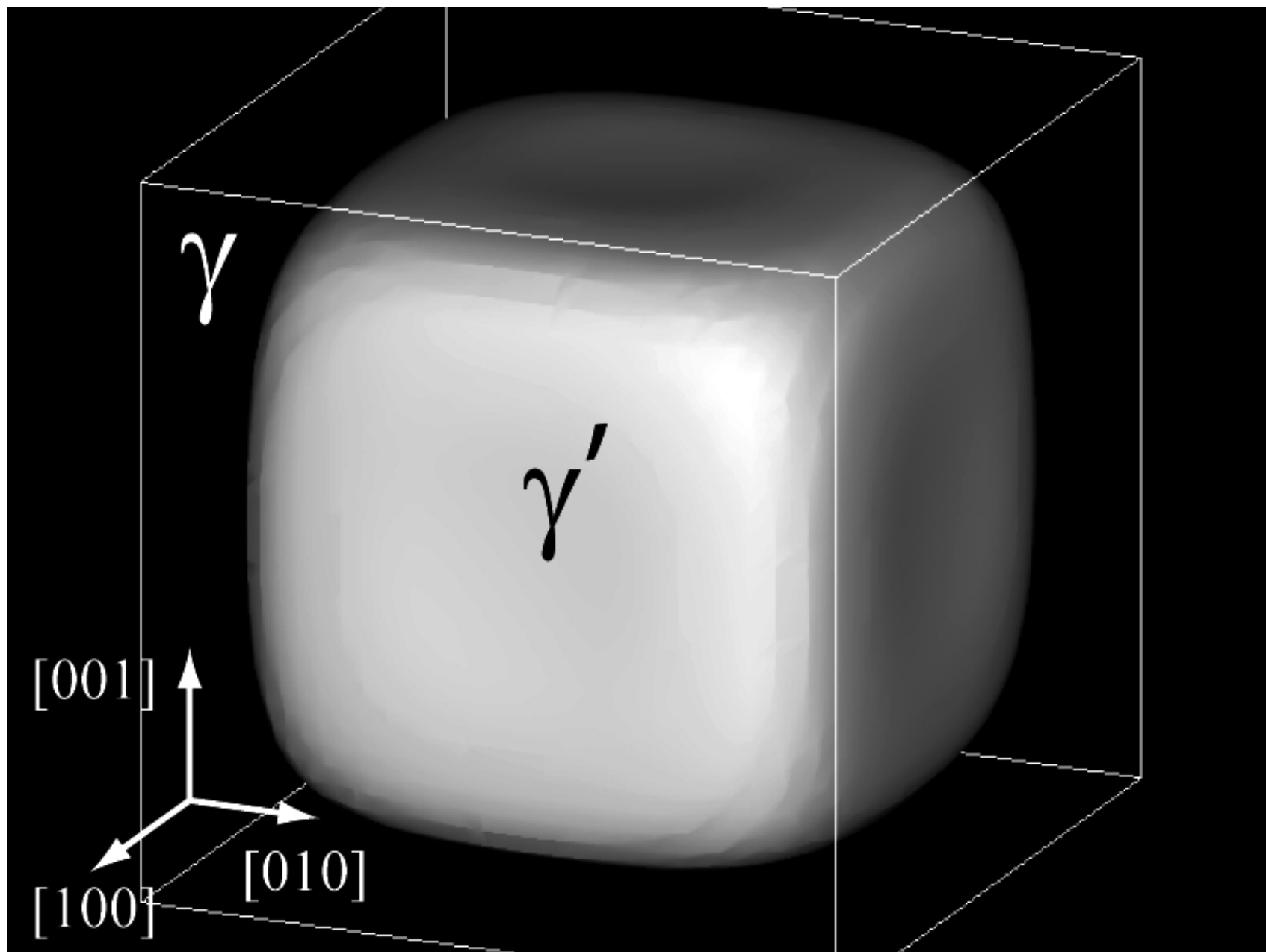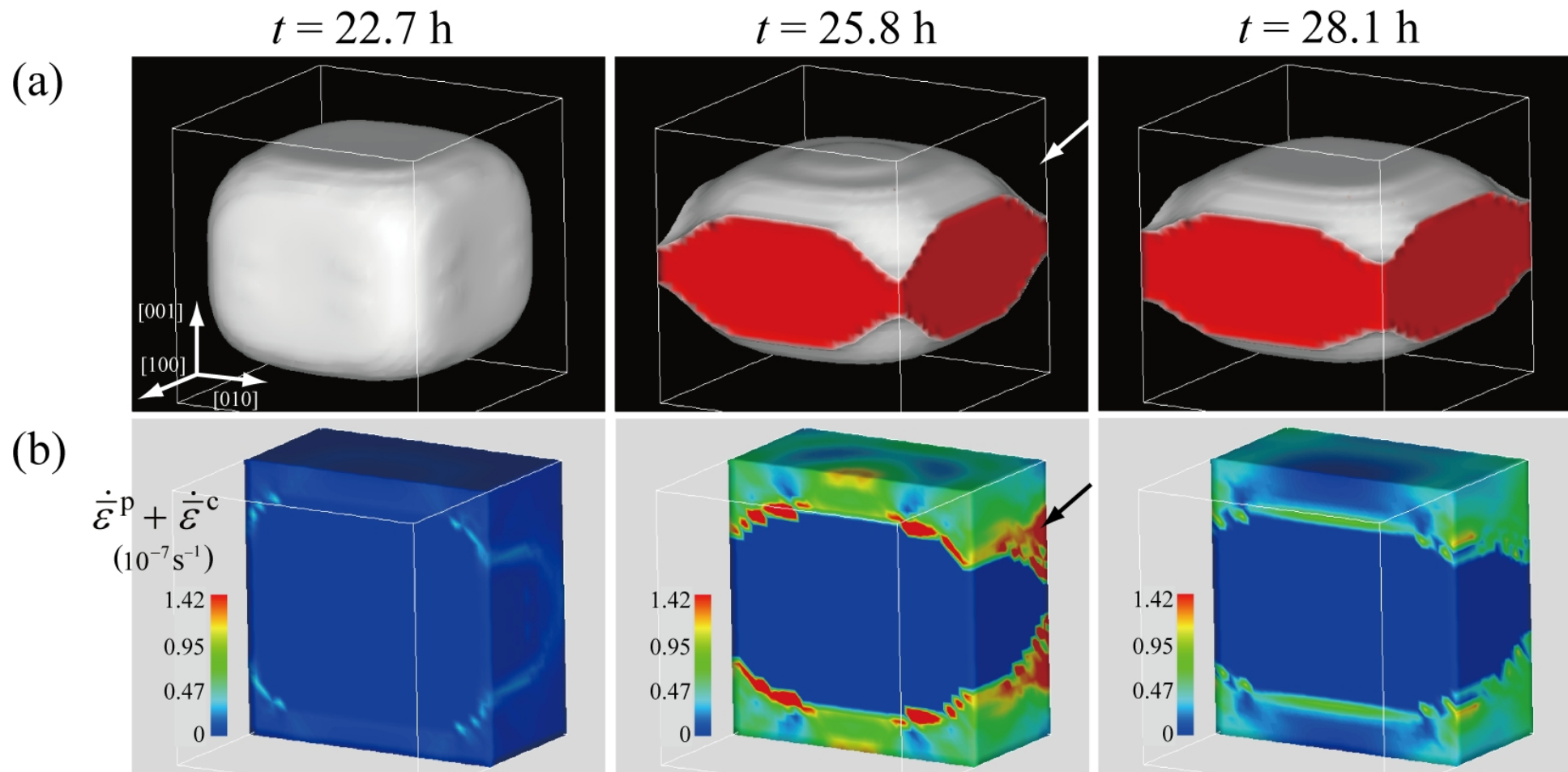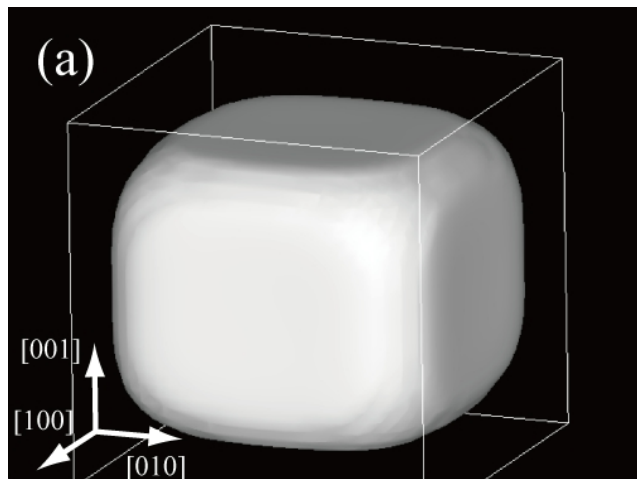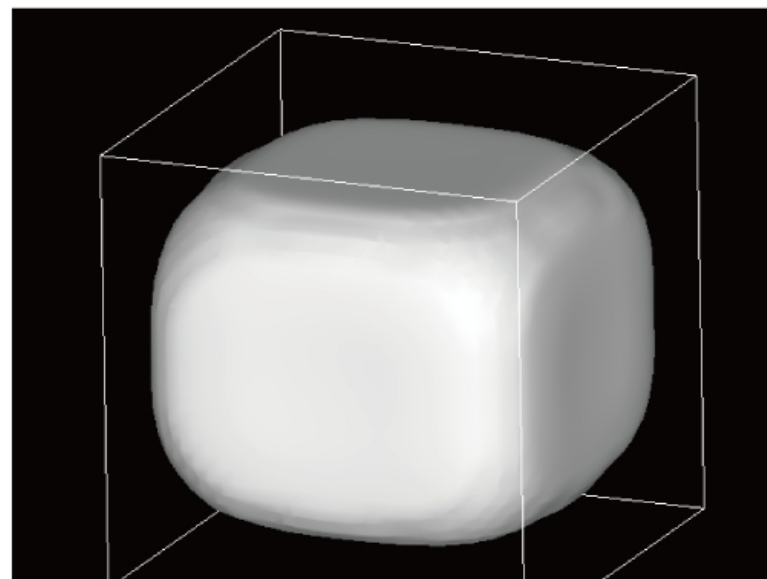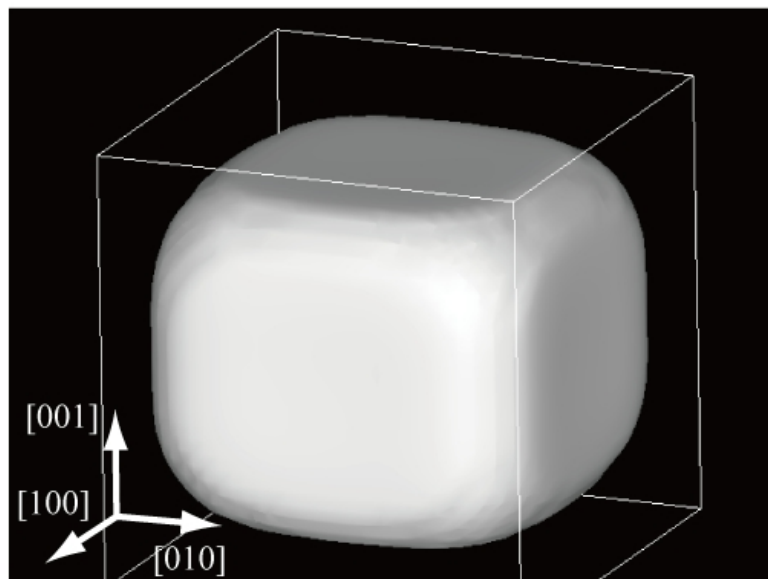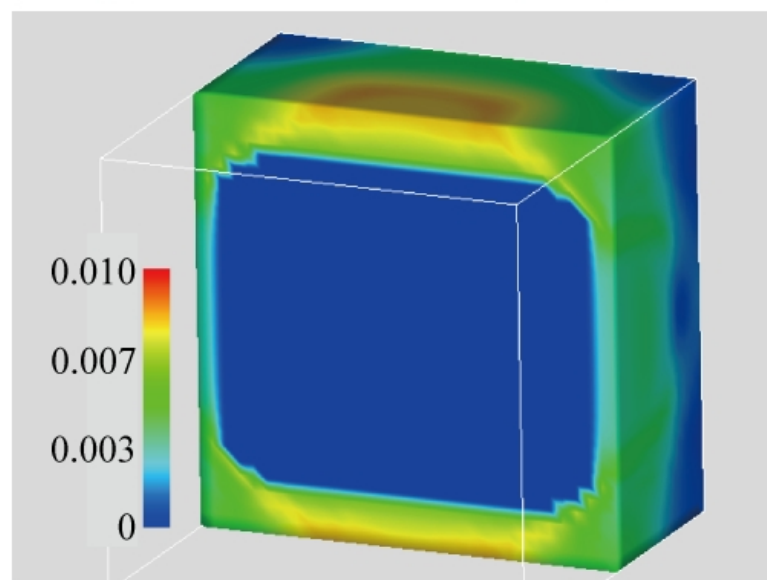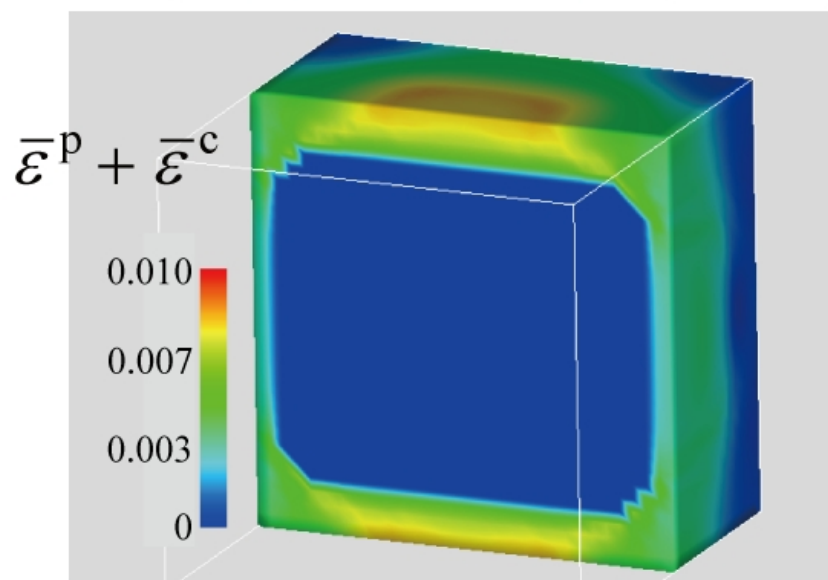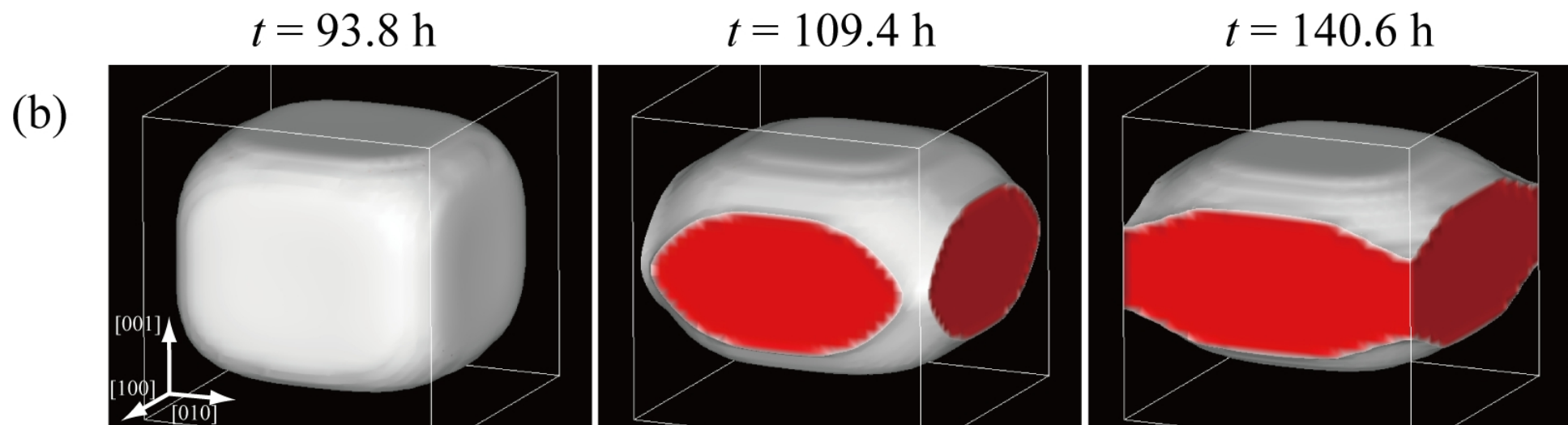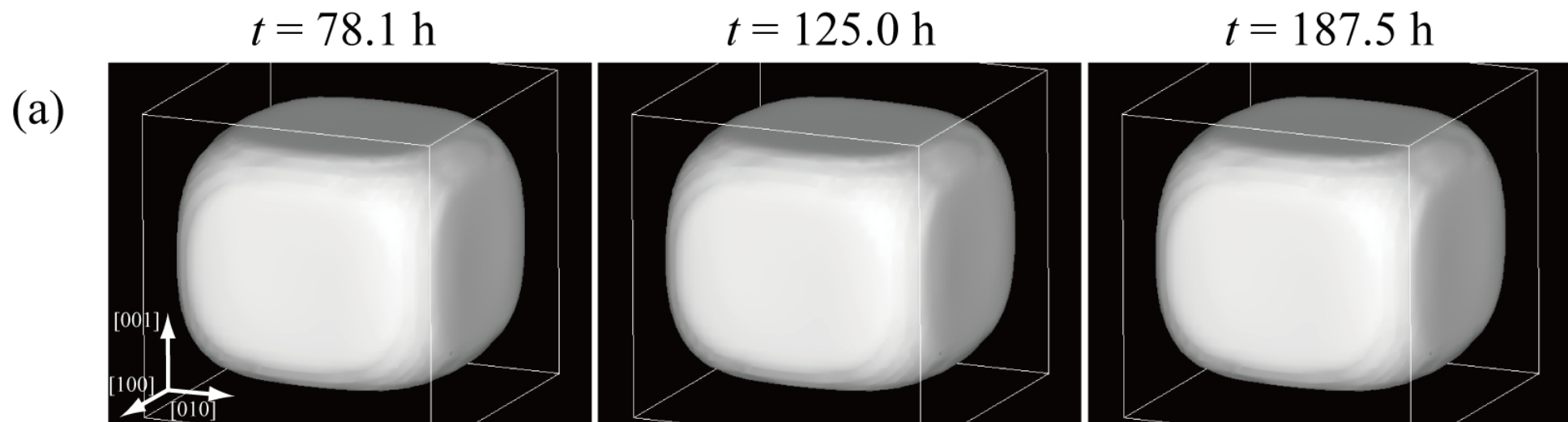
$t = 22.7$ h　　　　$t = 25.8$ h　　　　$t = 28.1$ h

(a)

[001]
[100]
[010]

(b)

$\dot{\overline{\varepsilon}}^{\,\mathrm{p}} + \dot{\overline{\varepsilon}}^{\,\mathrm{c}}$

$(10^{-7}\mathrm{s}^{-1})$

1.42
0.95
0.47
0

$t = 15.6$ h $t = 131.3$ h $t = 137.5$ h

(a)

[001]
[100]
[010]

(b)

$\dot{\bar{\varepsilon}}^{\mathrm{p}} + \dot{\bar{\varepsilon}}^{\mathrm{c}}$

$(10^{-8}\,\mathrm{s}^{-1})$

8.89
5.93
2.96
0

8.89
5.93
2.96
0

8.89
5.93
2.96
0

(a) 1273 K – 130 MPa

Creep rate, $\dot{\varepsilon}$ / s^{-1}

Time, t / h

□ CMSX-4
● Simulation

(b) 1273 K – 100 MPa

Creep rate, $\dot{\varepsilon}$ / s^{-1}

Time, t / h

□ CMSX-4
● Simulation

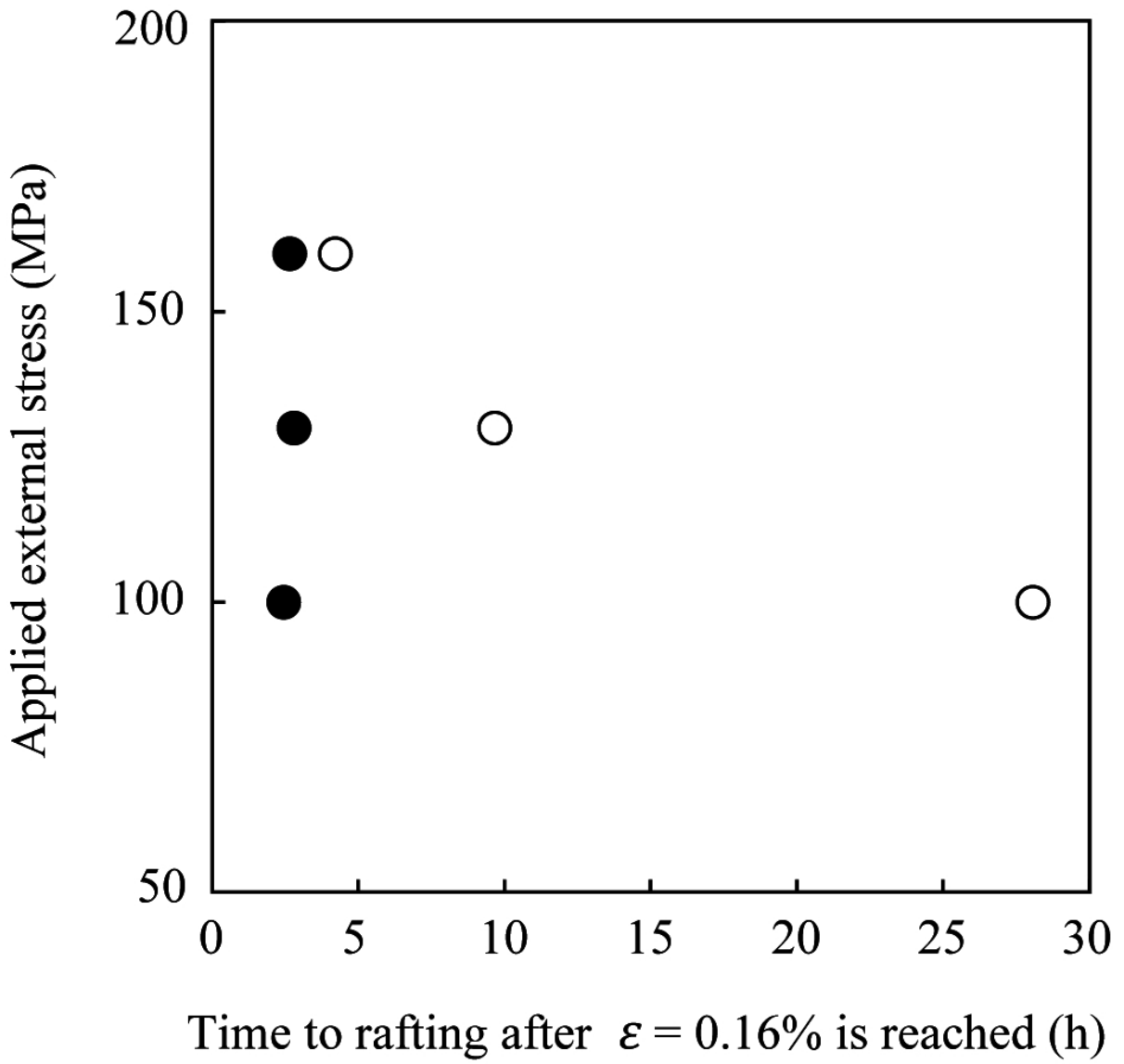$\varepsilon = 0.14\%$ ($t = 57.0$ h)　　　$\varepsilon = 0.16\%$ ($t = 103.2$ h)

(a)
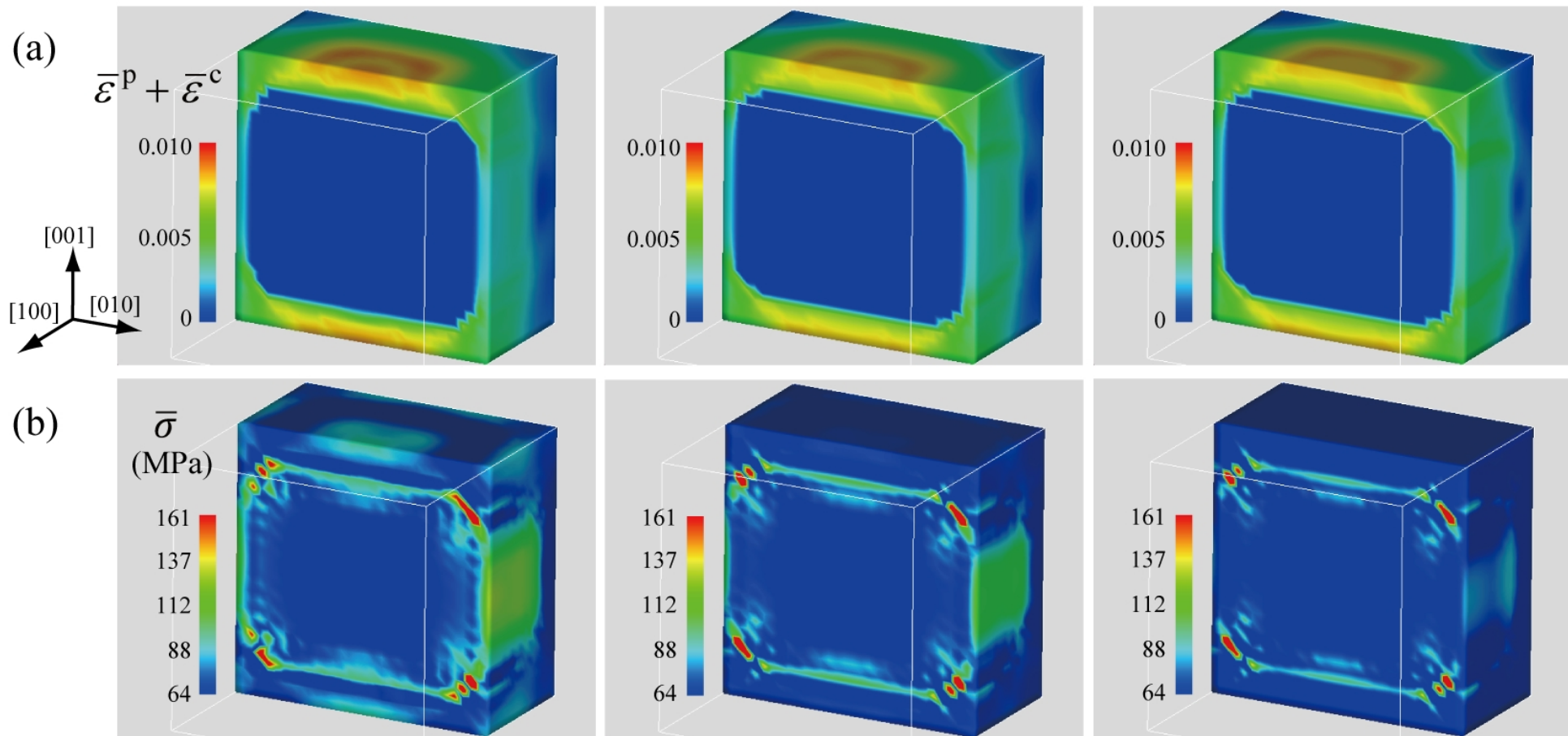
[001]

[100]

[010]

(b)

$\overline{\varepsilon}^{\mathrm{p}} + \overline{\varepsilon}^{\mathrm{c}}$

0.010

0.007

0.003

0

0.010

0.007

0.003

0

$t = 78.1$ h $t = 125.0$ h $t = 187.5$ h

(a)

[001]
[100]
[010]

$t = 93.8$ h $t = 109.4$ h $t = 140.6$ h
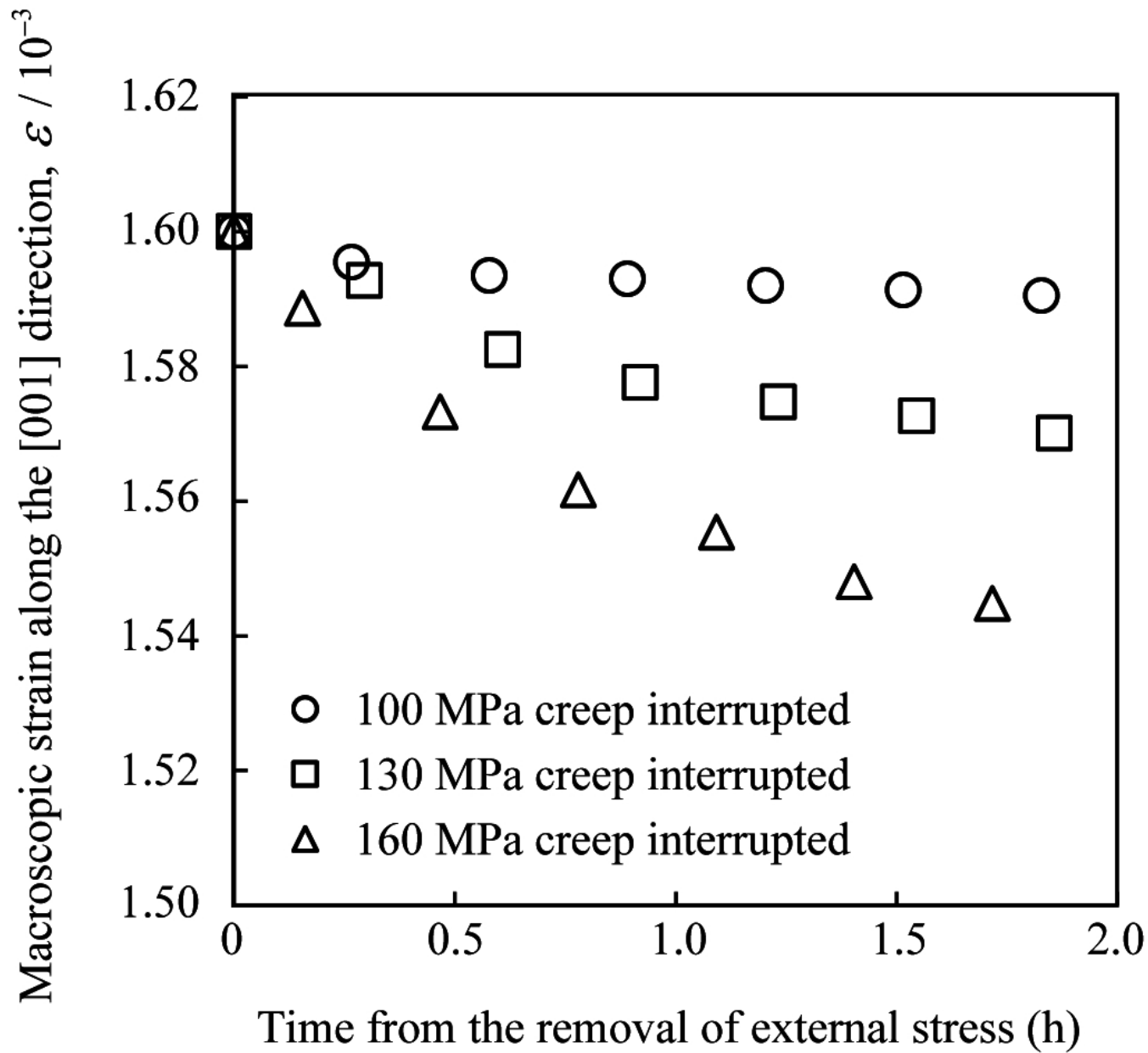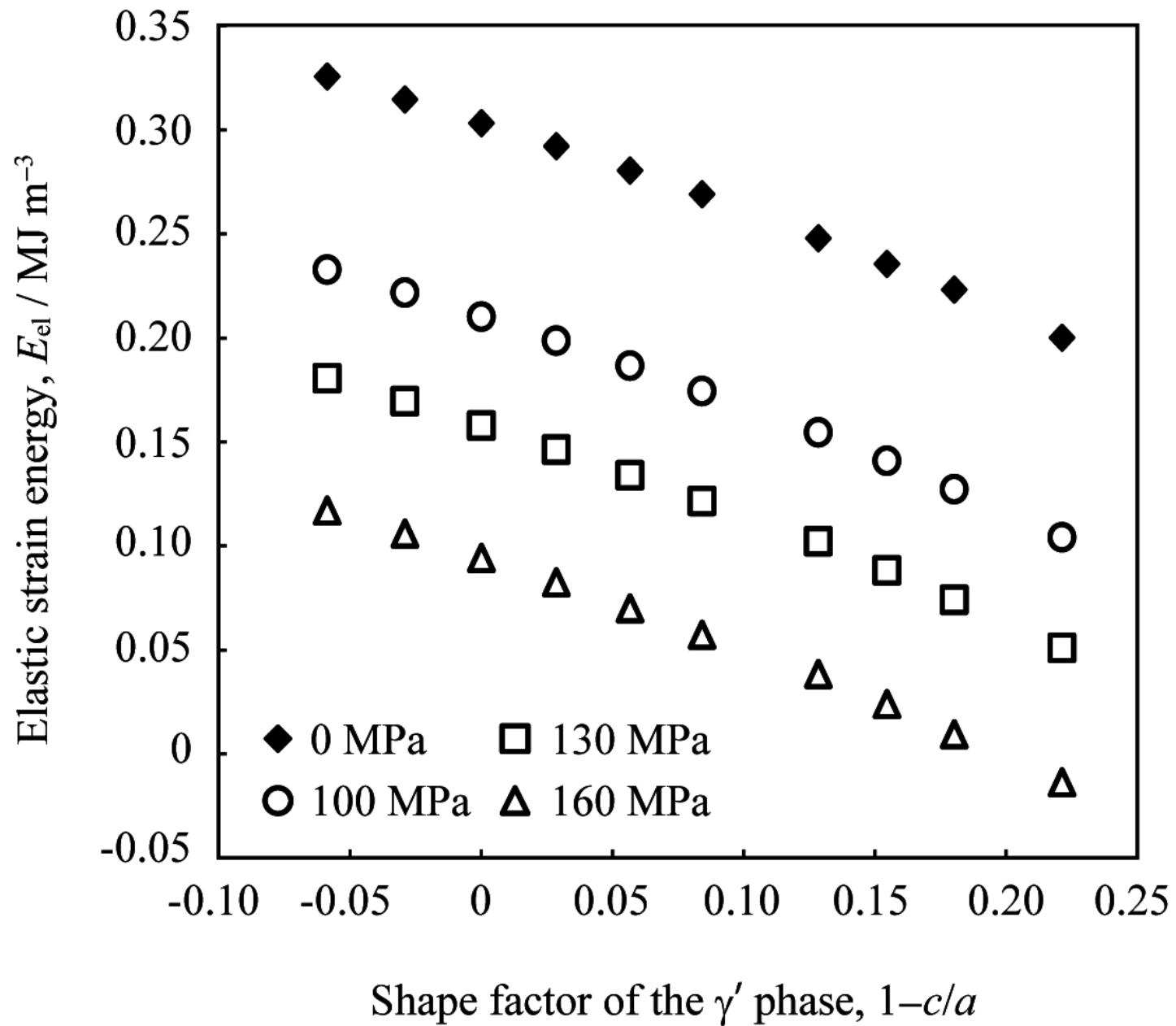
(b)

[001]
[100]
[010]

160 MPa creep interrupted ($\varepsilon = 0.16\%$)   130 MPa creep interrupted ($\varepsilon = 0.16\%$)   100 MPa creep interrupted ($\varepsilon = 0.16\%$)

(a) $\overline{\varepsilon}^{\mathrm{p}} + \overline{\varepsilon}^{\mathrm{c}}$

0.010
0.005
0

[001]
[100] [010]

(b) $\overline{\sigma}$ (MPa)

161
137
112
88
64

Figure axes:

Y-axis: Elastic strain energy, E_{el} / MJ m^{-3}

X-axis: Shape factor of the γ' phase, $1-c/a$

Legend:
- ◆ 0 MPa
- □ 130 MPa
- ○ 100 MPa
- △ 160 MPa
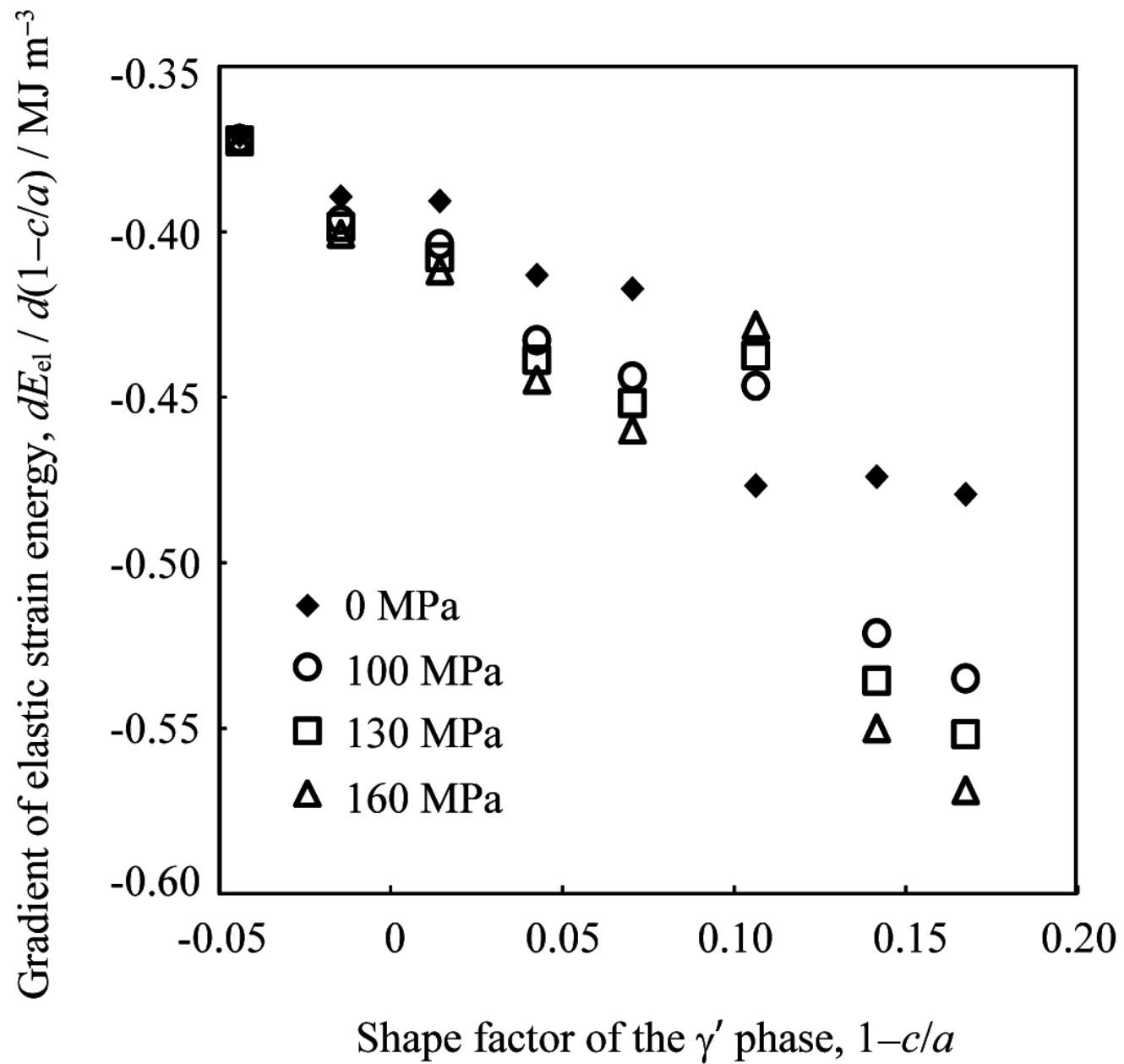
Highlights

- Directional coarsening (rafting) of the γ' phase is simulated at 1273 K.

- Time to rafting increases with decreasing magnitude of the applied external stress.

- Threshold value of macroscopic strain for inducing rafting is $\varepsilon_{th} = 0.12\%–0.16\%$.

- Rafting can be accelerated by the removal of external stress when $\varepsilon > \varepsilon_{th}$.